

# Diverse Similarity Encoder for Deep GAN Inversion

Cheng Yu, Wenmin Wang, *Senior Member, IEEE*,

**Abstract**—Current deep generative adversarial networks (GANs) can synthesize high-quality (HQ) images, so learning representation with GANs is favorable. GAN inversion is one of emerging approaches that study how to invert images into latent space. Existing GAN encoders can invert images on StyleGAN, but cannot adapt to other deep GANs. We propose a novel approach to address this issue. By evaluating diverse similarity in latent vectors and images, we design an adaptive encoder, named diverse similarity encoder (DSE), that can be expanded to a variety of state-of-the-art GANs. DSE makes GANs reconstruct higher fidelity images from HQ images, no matter whether they are synthesized or real images. DSE has unified convolutional blocks and adapts well to mainstream deep GANs, e.g., PGGAN, StyleGAN, and BigGAN.

**Index Terms**—Generative adversarial network (GAN), GAN encoder, GAN inversion, Image reconstruction.

## I. INTRODUCTION

WITH burgeoning advance of deep generative adversarial networks (GANs) [1], [2], [3], [4], high-quality (HQ) images can be generated with high resolutions of up to  $1024 \times 1024$  pixels, e.g., human face synthesis from deep GANs. Although StyleGAN1 [5] is often random and water-like droplets in synthesized images, and some image details always collapse when latent vectors deviate from the centre. Improved StyleGAN, e.g., StyleGAN2 [6], StyleGAN2-Ada [7], and StyleGAN3 [8], have alleviated the problem of water-like droplets in synthesized images. Similar to the conditional GAN (CGAN) [9], BigGAN [10] is another deep GAN for HQ image generation with image sizes of  $128 \times 128$ ,  $256 \times 256$ , and  $512 \times 512$ . It performs label-supervised training on ImageNet [11], which is a large-scale dataset with 1000 labels.

These deep GANs have good performances for image synthesis, indicating there is a room to discover GAN-based technologies for image editing tasks. Existing deep GANs, such as BigGAN and StyleGAN, design layer-wise latent vectors which well represent images. However, these GANs have no ability for inverting images to latent space.

Inverting images to latent space is called GAN inversion [12]. GAN-based works utilize inverted latent vectors to representation edited images or videos. Previous works [13], [14], [15] tried to design an encoder that trained with GANs for GAN inversion. Such methods perform well in shallow networks for low-quality images (below  $256 \times 256$ ), but cannot work well for deep GANs, which fail to invert HQ images into the latent space.

This work was supported by the Science and Technology Development Fund (FDCT) of Macau under Grant No. 0016/2019/A1 (corresponding author: Wenmin Wang).

Cheng Yu and Wenmin Wang are with School of Computer Science and Engineering, Macau University of Science and Technology, Macau 999078, China (e-mail: disanda@outlook.com; wmwang@must.edu.mo).

Code is available at: <https://github.com/disanda/DSE>.

For deep GAN inversion, as one of inversion methods for StyleGAN, Image2StyleGAN [16] optimizes style latent vectors  $w$  (size of [18,512]) which replaces the general latent vector  $z$  (size of [1,512]), but each image should be optimized independently to attain its corresponding  $w$ . In-Domain GAN [17] provides an encoder that trains with a discriminator to embed images into semantic vectors for GAN inversion. In addition, In-Domain GAN optimizes real image based on the encoder output. ALAE [18] designs an auto-encoder framework to upgrade StyleGAN and train it without pre-trained GANs to produce higher quality images with their reconstructions. pSp [19] directly trains an encoder with StyleGAN to invert images via face identity loss. For BigGAN inversion, drawing on the concept of BiGAN [13], BigBiGAN [20] improves the discriminator to judge image-latent pairs (rather than just judging images as in standard GANs) and trains the encoder with an upgraded BigGAN to obtain the BigGAN image reconstructions. However, the above methods only invert one deep GAN, and cannot match more deep GANs. Therefore, we aim to design an adaptive and robust encoder for deep GAN inversion.

We focus on GAN inversion via image reconstruction. Following [15], to transform GAN into an auto-encoder, we perform pre-trained GAN generators as decoders and design corresponding encoders. Inspired by [5], we design a general block that contains two convolutional layers. We try to match different deep GANs by fine-tuning the block. Finally, we reconstruct HQ synthesized and real images with high fidelity while improving and maintaining image qualities and semantic attributes. The contributions of our work can be summarized thus:

- For GAN inversion, we design a diverse similarity encoder (DSE) to adapt deep GANs. To better invert HQ images to latent vectors via DSE, we revisit diverse metrics for the similarity evaluation, and we design two sets of loss functions for training DSE.
- To reduce the size gap between images and latent vectors, we deal with different latent vectors to learn representation, and different scaled images to highlight the key areas of images. To scale HQ images, DSE deal with not only aligned images, but also mis-aligned images.
- We design a generalized and robust block to build DSE for matching different GANs. To the best of our knowledge, DSE is the first attempt that adapts well to current state-of-the-art deep GANs. Well-trained DSE with additional latent optimizations can reconstruct real images. Furthermore, using interpretable latent directions enables editing real images, e.g., human faces.



Fig. 1. The 1st row shows the face images synthesized by StyleGAN (FFHQ 1014 $\times$ 1024). The 2nd row shows GAN inversion results via DSE. Some inversion results are better in local details. The 3rd row shows inverted reconstructions (right) for 3 real images (left). Based on DSE, the 4th row shows edited results from 5 interpretable latent directions (mouth, eyeglasses, younger, older, and pose).

## II. RELATED WORK

### A. GAN Inversion

GAN inversion is an essential part of learning representation in GANs. Here, GAN inversion [12] aims to faithfully reconstruct images from latent vectors using GAN generators, i.e., let given images invert into latent space. Many GAN-based applications depend on GAN inversion, such as human face tasks [21], [22], [23], and animation synthesis[24], [25].

We sample latent vectors from latent space, which have also been called latent codes and latent variables. Traditional method [13] invert low-quality images into latent space via a shallow encoder. However, inverting HQ images into latent space is difficult. The image pixel size is too large, which is up to 1024  $\times$  1024 pixels. If the dimensionality of latent vectors is too small (e.g.,  $\leq 256$ ), this readily causes mode collapse or spatial entanglement in latent representation. So the GAN inversion becomes intricate due to the massive size gap between images and latent vectors. Although there are methods [26], [27] to reduce spatial entanglement by interpolating latent vectors in manifold directions, they only solve this problem in shallow GANs. Therefore, we reduce the gap by adding more scaled images and latent vectors, and we also evaluate the diverse similarity between HQ images and latent vectors for enhancing the performance.

In StyleGAN, there are additional style latent vectors ( $w$ ) in each convolution layer besides the typical latent vector (i.e.,  $z$  from the first layer input). Based on the layer-wise manner, Image2StyleGAN [16] directly optimize  $w$  with corresponding images for GAN inversion. However, the disadvantage of the method is that: getting  $w$  in any one image requires significant training operations (more than 10,000 epochs per image), making it less efficient when there are many real images

to invert. We consider an encoder to accomplish the GAN inversion.

Existing methods [17], [18], [19] have successfully inverted images to latent vectors via encoders. However, these works have only matched in one deep GAN and limited performance for reconstructing real and misaligned images. To address the problem, we design DST to enhance the GAN inversion performance of representation and generalization.

Finally, interpretable directions can be discovered on  $w$  via supervised methods [21], [28], which also can be discovered in unsupervised methods [29], [30], i.e., learning interpretable directions on GAN latent space for image editing.

### B. Similarity Evaluation

1) *LPIPS*: To measure the perceptual similarity of images, learned perceptual image patch similarity (LPIPS) requires a pre-trained model (e.g., VGG [31] or AlexNet [32]), which is trained from ImageNet [11] to extract multiple-layer features from images. LPIPS has been widely used to evaluate the similarity between images and their reconstructions. To better evaluate the similarity for HQ images, we add more different metrics to evaluate similarity.

2) *SSIM Index*: Reconstructed images are subject to inevitable distortions in deep neural networks, such as passing the down- or up-sampling layer, including the convolutional, normalization, pooling, and activation layers. Any of passing these layers may degrade the reconstruction quality. We consider adding SSIM [33] to measure jointly the perceptual feature similarity. SSIM has high computational efficiency and does not require pre-training models.

3) *Grad-CAM*: Zhou et al. [34] proposed an approach called class activation mapping (CAM) to locate target positions within images using the ImageNet model. However, to

obtain locations, CAM needs to train the model again, which removes the fully connected layers from the model output. Gradient-weighted class activation mapping (Grad-CAM) [35] upgrades CAM by utilizing a pre-trained model gradient at the pixel level and does not require retraining the model. We use Grad-CAM to scale images so that we evaluate similarity while more focusing on the key image targets.

Existing methods evaluating the image similarity are limited in metrics. In fact, using more diverse similarity metrics for deep GAN inversion is deserved, because evaluating high HQ images is difficult. Compared to LPIPS, SSIM has higher computational efficiency, adding SSIM gives a better indication of encoder training. Consequently, we combine diverse similarity as a loss function to train DSE for matching deep GANs.

For deep GAN inversion, only evaluating the similarity of image pixels is insufficient, especially on misaligned images. So the inversion should evaluate corresponding latent vectors. One reason is that the image and latent vector sizes are too far apart. Latent vectors cannot map images well. We evaluate different latent vectors for higher accurate representation and also evaluate the key area similarity of images to enhance the inversion performance.

### III. DIVERSE SIMILARITY ENCODER

Our approach is summarized here: we evaluate the diverse similarity of images and corresponding latent vectors, where we evaluate different scaled images to highlight image key areas and evaluate latent vectors to enhance the latent representation.

For evaluating latent vectors, three metrics are used: mean square error (MSE), cosine similarity (COS) and Kullback–Leibler divergence (KL, also called information divergence). For evaluating images, we add two metrics to measure the feature similarity: SSIM and LPIPS.

#### A. Latent Vectors

In GANs and auto-encoders, we utilize latent vectors which sample from latent space to represent synthesized images. We denote the latent vector as  $\mathbf{z}$ , which obeys the Gaussian distribution. We briefly regard the synthesized image as the pixel vector and denote the vector as  $\mathbf{x}$ . Moreover, we denote the ground truth image as  $\mathbf{y}$ , i.e., the real image.  $\mathbf{z}'$  denotes the inverted vector, which outputs from encoders and reconstructs synthesized images;  $\mathbf{x}'$  denotes the image reconstruction. Finally,  $E$  denotes the GAN encoder and  $G$  denotes the GAN generator.

We design the loss function combined images (IMG) and latent vectors (LV) as follows:

$$\mathcal{L}_E = \mathcal{L}_{LV}(\mathbf{z}, \mathbf{z}') + \mathcal{L}_{IMG}(\mathbf{x}, \mathbf{x}'). \quad (1)$$

Where  $\mathbf{x}$  can be changed as  $\mathbf{y}$  and let the latent vector  $\mathbf{z}$  changes to a learnable vector for inverting real image to latent space.

(N, C, H, W) denotes the image size, where N is training batch size; C is image channels, H is height and W is weight. (N, D) denotes latent size, where D is the latent dimensionality.

To upgrade the encoder weights, we evaluate the similarity in the vector pairs:  $(\mathbf{x}, \mathbf{x}')$  and  $(\mathbf{z}, \mathbf{z}')$ . If the vector size is:  $\mathbf{z} \ll \mathbf{x}$ , the joint evaluation is too intricate to perform.

Following [16], too small size latent vectors cannot represent HQ images, such as the  $\mathbf{z}$  size is small than  $(n, 512)$ , which cannot represent HQ images which size is  $(n, 3, 1024, 1024)$ .

Similar to existing works in StyleGAN [5], [18], [16], [19], [17], we choose StyleGAN-based latent vectors to design our encoder. we evaluate the similarity of  $\mathbf{w}$ :  $(n, n_{layers}, 512)$  in place of  $\mathbf{z}$ :  $(n, 512)$ .  $n_{layers}$  denotes the number of style fully-connected layers, so  $\mathbf{w}$  is a layer-wise vector, e.g.,  $1024 \times 1024$  faces need  $\mathbf{w}$ :  $(n, 18, 512)$ .

We consider two other types of latent vectors that have different sizes to represent images jointly, so we can reduce the size gap between HQ images and latent vectors. One is constant vectors  $\mathbf{z}_c$ , where the size of  $\mathbf{z}_c$  is  $(n, 512, 4, 4)$ .  $\mathbf{z}_c$  is used to first block the input in StyleGAN'  $G$ , where the size of  $\mathbf{z}_c$  is larger than the general GAN input size  $\mathbf{z}$ :  $(n, 512)$ . [5] indicates that  $\mathbf{z}_c$  enhances the stability of the training process.

The other one is the layer-lever noise vector  $\mathbf{z}_n$ , which is performed as learnable parameters on each convolutional layer, where  $\mathbf{z}_n$  is of size  $(n, n_{layers}, n_{channels})$ .  $n_{channels}$  represents the number of input channels for each convolutional layer.  $\mathbf{z}_n$  affects the peripheral areas slightly, e.g., the hair local diversification in human faces, so  $\mathbf{z}_n$  produces the diversity of the local representation.

We design the encoder which output  $\mathbf{z}'_c$  and attached learnable  $\mathbf{z}'_n$  in convolutional layers. That is an incremental trick to keep a symmetric architecture between  $E$  and  $G$ .

There are 3 latent vector pairs  $(\mathbf{w}, \mathbf{w}')$ ,  $(\mathbf{z}_c, \mathbf{z}'_c)$ , and  $(\mathbf{z}_n, \mathbf{z}'_n)$  for training  $E$ . Let  $E$  output  $\mathbf{w}'$ ,  $\mathbf{z}'_c$ , and upgrade  $\mathbf{z}'_n$ , then we evaluate the latent similarity and optimize  $E$  as following loss function:

$$\mathcal{L}_{LV} = \mathcal{L}_{LV}(\mathbf{w}, \mathbf{w}'). \quad (2)$$

Where we only evaluate  $\mathbf{w}$  in latent space. We measure the latent similarity via the diverse metrics: MSE and COS. The loss functions are summarized as follows:

$$\begin{aligned} \mathcal{L}_{LV}(\mathbf{w}, \mathbf{w}') &= \mathcal{L}_{MSE}(\mathbf{w}, \mathbf{w}') + \mathcal{L}_{COS}(\mathbf{w}, \mathbf{w}') \\ &= \frac{\|\mathbf{w} - \mathbf{w}'\|_2}{n} + 1 - \frac{\mathbf{w} \cdot \mathbf{w}'}{\|\mathbf{w}\|_2 \times \|\mathbf{w}'\|_2}. \end{aligned} \quad (3)$$

In addition, we analyze vector similarity from a statistical perspective, i.e.,  $\mathbf{w}$  and  $\mathbf{w}'$  are the same distribution (i.i.d.). We evaluate the distribution similarity via KL. We use an activation function (SoftMax,  $\mathcal{S}$ ) to perform it: Let latent vectors pass  $\mathcal{S}$  when using KL (see Eq. 4) as:

$$\mathcal{L}_{KL}(\mathbf{w}, \mathbf{w}') = - \sum \mathcal{S}(w') \log \frac{\mathcal{S}(w)}{\mathcal{S}(w')}, \quad (4)$$

Where  $w$  and  $w'$  are the point-wise unit of  $\mathbf{w}$  and  $\mathbf{w}'$  respectively. We summarize the joint loss functions that measure the LV similarity as:

$$\mathcal{L}_{LV} = \mathcal{L}_{KL} + \alpha \mathcal{L}_{MSE} + \beta \mathcal{L}_{COS}. \quad (5)$$

Where  $\alpha$  and  $\beta$  are hyper parameters. Even though we have expanded latent vectors to reduce the size gap between images and latent space, we do not evaluate the similarity of other two latent vectors ( $\mathbf{z}'_c$  and  $\mathbf{z}'_n$ ). The size gap is still large for training encoders, so we additionally consider reducing the size gap via scaled images.

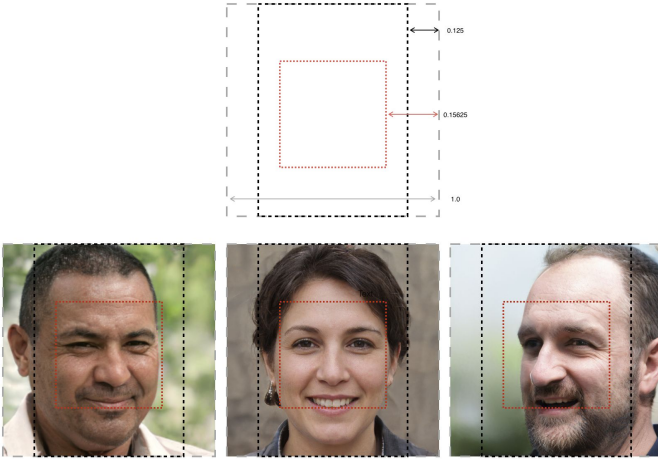


Fig. 2. Three-scale images for centre-aligned faces. Gray dashed line is the original scale; black dashed line scales AT1; red dashed line scales AT2.

### B. Three-scale Images

It is difficult to map HQ images to latent space while maintaining a high-fidelity reconstructed image. Feature information is inevitably lost in the process of encoding and decoding. The most common phenomenon is that local details become different in reconstructed images. Therefore, we propose three-scale areas (TSA) to highlight the image key areas.

We denote original images as the first scaled area; We add two different scaled areas:  $(\mathbf{x}_1, \mathbf{x}'_1)$  and  $(\mathbf{x}_2, \mathbf{x}'_2)$ . The two new areas are outstanding attentions for original images, which further reduces the feature size between image and latent vectors. To simplify, AT1 denotes the first attention:  $\mathbf{x}_1, \mathbf{x}'_1 = AT1(\mathbf{x}, \mathbf{x}')$ . Based on AT1, AT2 denotes the second attention:  $\mathbf{x}_2, \mathbf{x}'_2 = AT2(\mathbf{x}, \mathbf{x}')$ . The two attentions are scaled for outstanding key positions in HQ images. The loss function is given as:

$$\mathcal{L}_{IMG}(\mathbf{x}, \mathbf{x}') \rightarrow \mathcal{L}_{IMG}((\mathbf{x}, \mathbf{x}'), \mu_1(\mathbf{x}_1, \mathbf{x}'_1), \mu_2(\mathbf{x}_2, \mathbf{x}'_2)). \quad (6)$$

Where  $\mu_1$  and  $\mu_2$  are hyper parameters. For preprocessed images, e.g., faces from CeleBA-HQ [36]), they are centre-aligned. Thus, TSA is easy for aligned images: scaling fixed areas. As shown in Fig. 2, AT1 crop along with the black dashed line and AT2 crop along red dashed line. We set the hyper parameters empirically as  $\mu_1 = 0.375$  and  $\mu_2 = 0.625$  for aligned faces (Centre-aligned TSA).

To locate targets in misaligned images, we use Gram-CAM-based TSA. As shown in Fig. 3, we input images into a VGG16 [31] model, which contains 5 blocks with 13 convolutional layers pre-trained from the ImageNet classification. We extract the gradient values from the last convolutional layer to

generate image heat maps, and the process denotes as AT1; these maps highlight target positions. Furthermore, we label the targets in image pixels and get the labelled images, and denote the process as AT2.

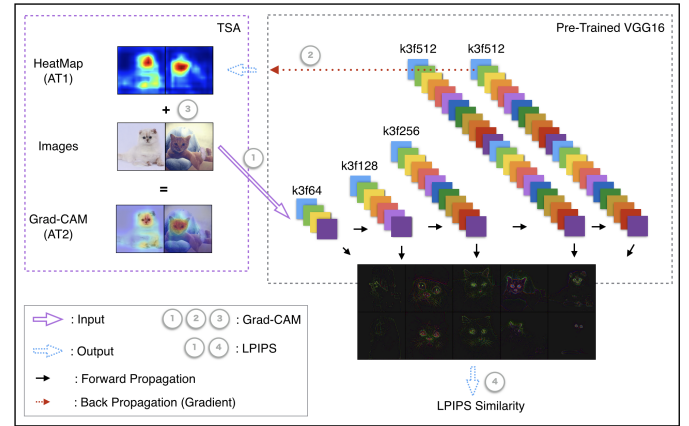


Fig. 3. Three scales for misaligned images. Besides origin scaled images. The first attentions are the target heat maps obtained from VGG16 (AT1), and the second attentions are labelled images (AT2).

Apart from latent vectors, we add two metrics to evaluate the image similarity: LPIPS [37] and SSIM [33]. We combine Gram-CAM and LPIPS to use the same ImageNet model (VGG16). LPIPS comes from forwarding propagation, and Grad-CAM comes from back-propagation.

We select the final convolutional layer in each block of the VGG16 model to extract image features; then we measure the feature similarity for LPIPS scores. Next, we directly use [33] to acquire SSIM scores. The loss function of the image part follows the diverse similarity evaluation:

$$\mathcal{L}_{IMG} = \mathcal{L}_{KL} + \alpha \mathcal{L}_{MSE} + \beta \mathcal{L}_{COS} + \gamma \mathcal{L}_{LPIPS} + \delta \mathcal{L}_{SSIM}. \quad (7)$$

Where  $\gamma$  and  $\delta$  are hyper parameters. Finally, the loss function for DSE can be briefly summarized as:

$$\mathcal{L}_{DSE} = \mathcal{L}_{IMG} + \epsilon \mathcal{L}_{LV}. \quad (8)$$

We set all hyper parameters empirically as:  $\alpha = 5$ ,  $\beta = 3$ ,  $\gamma = 2$ ,  $\delta = 1$  and  $\epsilon = 0.01$ .

### C. Encoder Implementation

We illustrate the data flow of DSE in Fig 4 (with the case of StyleGAN). The architecture of  $E$  is symmetric to  $G$ .  $(\mathbf{w}, \mathbf{z}_c)$  input to  $G$  and  $(\mathbf{w}', \mathbf{z}'_c)$  output from  $E$ .  $\mathbf{z}_n$  and  $\mathbf{z}'_n$  are learnable parameters from  $G$  and  $E$  respectively.

The block of  $E$  is shown in Fig. 5. Inspired by [38], we design a residual bypass in each block, where the block architecture contains two convolutional layers (CONV). Based on CONV, noise vector  $\mathbf{z}'_n$  is learnable weight and layer-wise style vector  $\mathbf{w}'$  output from fully connected layers (FC). FC and CONV are based on an equalized learning rate [3]. We initialize the weights using the Xavier norm [39]. The details of the entire architecture of  $E$  are given in Table I (for StyleGAN).

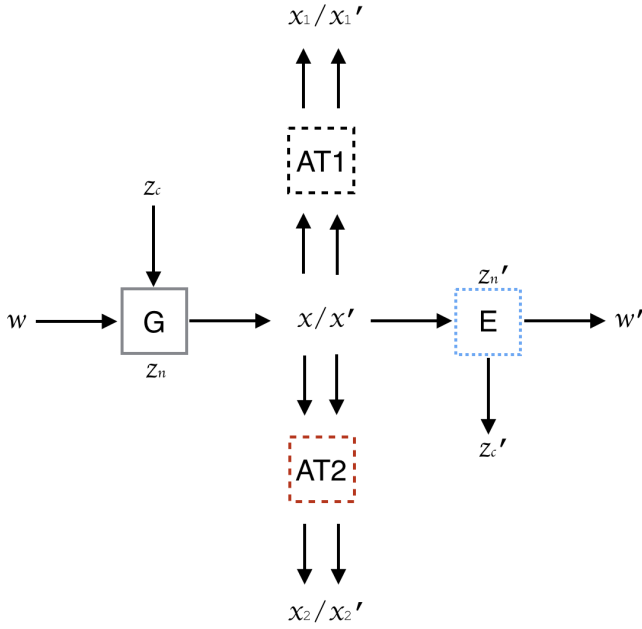


Fig. 4. Data flow of DSE.

To implement PGGAN, we remove the style- and noise-related vectors (i.e.,  $\mathbf{w}'$  and  $\mathbf{z}'_n$ ), and remove style FC in each block. At the last block, we change the last CONV to an FC to adapt to PGGAN. Distinct from StyleGAN, the latent vector of PGGAN is  $\mathbf{z} \in \mathbb{R}^{512}$  from the first layer.

To implement BigGAN, we also remove  $\mathbf{w}'$ ,  $\mathbf{z}'_n$  with relevant layers from each block. We replace the instance norm with the conditional batch normalization (CBN).  $\mathbf{c} \in \mathbb{R}^{256}$  denotes ImageNet labels that input into  $G$  to synthesize the label-based image. Similar to  $\mathbf{w}$ ,  $\mathbf{c}$  is a layer-wise vector and its imitated vector is  $\mathbf{c}'$ .

In the last block of BigGAN, two FC layers output  $\mathbf{c}'$  and  $\mathbf{z} \in \mathbb{R}^{128}$  separately. We perform the label vectors as one-hot vectors. Additional architecture details for  $E$  (PGGAN and BigGAN) are reported in Table II.

#### D. Training Setup

Training DSE is performed in a self-supervised manner. A large number of random samples ( $\mathbf{z}$ ) is used to synthesize images:  $G(\mathbf{z}) \simeq \mathbf{x}$ . First, we evaluate the similarity of  $\mathbf{x}$  with its reconstruction  $\mathbf{x}' \simeq G(E(G(\mathbf{z})))$ .  $(\mathbf{x}_1, \mathbf{x}'_1)$  and  $(\mathbf{x}_2, \mathbf{x}'_2)$  are resized to the same size of  $(\mathbf{x}, \mathbf{x}')$ .

To summarize the implementation, we present the details in Algorithm 1 as case of StyleGAN. Here, we use the general latent vector  $\mathbf{z} \in \mathbb{R}^{512}$ , which input into the mapping model  $M$  to obtain  $\mathbf{w} \in \mathbb{R}^{512 \times n_{layers}}$ .

There are two training strategies as below:

Strategy 1, we set  $\mu_1 = 1$  and  $\mu_2 = 1$  (see Eq. 7). Here, we only use two scaled attentions to improve the performance. To save GPU memory, we removed the gradients of image pixels under backward propagation.

Strategy 2, we set  $\mu_1 = 5$  and  $\mu_2 = 9$  and add a fused scale operation in each block, which are used in PGGAN [3].

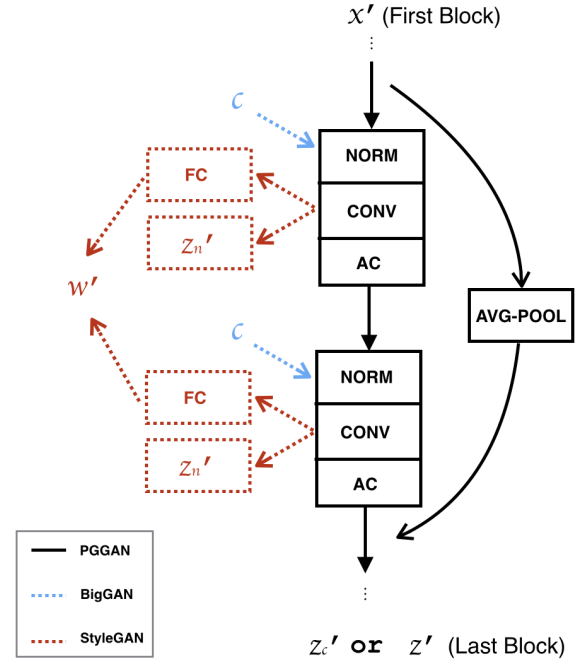


Fig. 5. Architecture overview of DSE one-block. NORM denotes normalization layer; AC denotes activation layer. FC and learnable  $\mathbf{z}'_n$  are not implemented in PGGAN and BigGAN.

---

#### Algorithm 1 Training DSE

---

**Input:**  $\mathbf{z}, \mathbf{z}_c, \mathbf{z}_n$ . **Frozen weights:**  $G, M$ .

**Optimizing:**  $E$  weights  $\rightarrow \mathbf{w}_E$

---

#### Begin:

- 1: **while** Epochs **do**
- 2:   Sample:  $\mathbf{z} \sim N(0, 1)$ .
- 3:   Forward Nets:  $\mathbf{w} = M(\mathbf{z}), \mathbf{x}, \mathbf{z}_c = G(\mathbf{w})$ .
- 4:   Scaled Attentions :  $\mathbf{x}_1 = AT_1(\mathbf{x}), \mathbf{x}_2 = AT_2(\mathbf{x})$ .
- 5:   **if**  $\mathbf{x} \sim G(E(\mathbf{x}))$  **then**
- 6:     Return.
- 7:   **else**
- 8:      $\mathbf{x}' = G(E(\mathbf{x})), \mathbf{x}'_1 = AT_1(\mathbf{x}'), \mathbf{x}'_2 = AT_2(\mathbf{x}')$ .
- 9:      $\mathbf{w}', \mathbf{z}'_c, \mathbf{z}'_n = E(G(E(\mathbf{x})))$ .
- 10:     $\nabla \mathcal{L}_1 \leftarrow \mathcal{L}_{IMG}((\mathbf{x}, \mathbf{x}'), \mu_1(\mathbf{x}_1, \mathbf{x}'_1), \mu_2(\mathbf{x}_2, \mathbf{x}'_2))$
- 11:     $\nabla \mathcal{L}_2 \leftarrow \mathcal{L}_{LS}((\mathbf{w}, \mathbf{w}'))$
- 12:     $\mathbf{w}_E \leftarrow \mathbf{w}_E + \nabla \mathcal{L}_1 + \epsilon \nabla \mathcal{L}_2$
- 13:    **end if**
- 14: **end while**

#### End

---

Larger  $(\mu_1, \mu_2)$  gives slightly better performances on attention regions.

Strategy 2 keeps all gradients, and reconstructed images are more faithful to the original images (with a slight blur in image margins); however, keeping attention gradients will increase the training cost, increased around 20 percent of gradient memory and consumption. In strategy 1, DSE optimizes from other similar synthesized images. But in strategy 2, DSE optimizes from noise and then turn to blurred images (see the difference of the two strategies at Fig. 6).

TABLE I  
DSE ARCHITECTURES FOR STYLEGAN AND PGGAN.

Block ID Res.	StyleGAN Encoder ( $E$ )		
	256×256	512×512	1024×1024
1 4×4	FC, IN, CONV(64,64,3), $\mathbf{z}'_n$ , L-ReLU	FC, IN, CONV(32,32,3), $\mathbf{z}'_n$ , L-ReLU	FC, IN, CONV(16,16,3), $\mathbf{z}'_n$ , L-ReLU
	FC, IN, CONV(64,128,3), $\mathbf{z}'_n$ , L-ReLU	FC, IN, CONV(32,64,3), $\mathbf{z}'_n$ , L-ReLU	FC, IN, CONV(16,32,3), $\mathbf{z}'_n$ , L-ReLU
2 8×8	FC, IN, CONV(128,128,3), $\mathbf{z}'_n$ , L-ReLU	FC, IN, CONV(64,64,3), $\mathbf{z}'_n$ , L-ReLU	FC, IN, CONV(32,32,3), $\mathbf{z}'_n$ , L-ReLU
	FC, IN, CONV(128,256,3), $\mathbf{z}'_n$ , L-ReLU	FC, IN, CONV(64,128,3), $\mathbf{z}'_n$ , L-ReLU	FC, IN, CONV(32,64,3), $\mathbf{z}'_n$ , L-ReLU
3 16×16	FC, IN, CONV(256,256,3), $\mathbf{z}'_n$ , L-ReLU	FC, IN, CONV(128,128,3), $\mathbf{z}'_n$ , L-ReLU	FC, IN, CONV(64,64,3), $\mathbf{z}'_n$ , L-ReLU
	FC, IN, CONV(256,512,3), $\mathbf{z}'_n$ , L-ReLU	FC, IN, CONV(128,256,3), $\mathbf{z}'_n$ , L-ReLU	FC, IN, CONV(64,128,3), $\mathbf{z}'_n$ , L-ReLU
4 32×32	FC, IN, CONV(512,512,3), $\mathbf{z}'_n$ , L-ReLU	FC, IN, CONV(256,256,3), $\mathbf{z}'_n$ , L-ReLU	FC, IN, CONV(128,128,3), $\mathbf{z}'_n$ , L-ReLU
	FC, IN, CONV(512,512,3), $\mathbf{z}'_n$ , L-ReLU	FC, IN, CONV(256,512,3), $\mathbf{z}'_n$ , L-ReLU	FC, IN, CONV(128,256,3), $\mathbf{z}'_n$ , L-ReLU
5 64×64	FC, IN, CONV(512,512,3), $\mathbf{z}'_n$ , L-ReLU	FC, IN, CONV(512,512,3), $\mathbf{z}'_n$ , L-ReLU	FC, IN, CONV(256,256,3), $\mathbf{z}'_n$ , L-ReLU
	FC, IN, CONV(512,512,3), $\mathbf{z}'_n$ , L-ReLU	FC, IN, CONV(512,512,3), $\mathbf{z}'_n$ , L-ReLU	FC, IN, CONV(256,512,3), $\mathbf{z}'_n$ , L-ReLU
6 128×128	FC, IN, CONV(512,512,3), $\mathbf{z}'_n$ , L-ReLU	FC, IN, CONV(512,512,3), $\mathbf{z}'_n$ , L-ReLU	FC, IN, CONV(512,512,3), $\mathbf{z}'_n$ , L-ReLU
	FC, IN, CONV(512,512,3), $\mathbf{z}'_n$ , L-ReLU	FC, IN, CONV(512,512,3), $\mathbf{z}'_n$ , L-ReLU	FC, IN, CONV(512,512,3), $\mathbf{z}'_n$ , L-ReLU
7 256×256	FC, IN, CONV(512,512,3), $\mathbf{z}'_n$ , L-ReLU	FC, IN, CONV(512,512,3), $\mathbf{z}'_n$ , L-ReLU	FC, IN, CONV(512,512,3), $\mathbf{z}'_n$ , L-ReLU
	FC(1024,512)	FC, IN, CONV(512,512,3), $\mathbf{z}'_n$ , L-ReLU	FC, IN, CONV(512,512,3), $\mathbf{z}'_n$ , L-ReLU
8 512×512		FC, IN, CONV(512,512,3), $\mathbf{z}'_n$ , L-ReLU	FC, IN, CONV(512,512,3), $\mathbf{z}'_n$ , L-ReLU
		FC(1024,512)	FC, IN, CONV(512,512,3), $\mathbf{z}'_n$ , L-ReLU
9 1024×1024			FC, IN, CONV(512,512,3), $\mathbf{z}'_n$ , L-ReLU
			FC(1024,512)

\* In block 1, CONV(3,  $C_{in}$ , 1) is not shown in the table, which maps the RGB channels to  $C_{in}$ .

\* In CONV( $C_{in}$ ,  $C_{out}$ ,  $K$ ),  $C_{in}$  is the input channel,  $C_{out}$  is output channels, and  $K$  is kernel size. Stride and padding are 1 for all CONVs.

\* FC outputs layer-wise style vectors of  $\mathbf{w}'$ . IN is instance normalization [40], L-ReLU is the activation function of Leaky ReLU.

\* For PGGAN,  $G$  inputs  $\mathbf{z} \in \mathbb{R}^{512}$ .  $E$  outputs its imitated vector:  $\mathbf{z}' \in \mathbb{R}^{512}$ . We remove all FC and  $\mathbf{z}'_n$ , then add FC(1024\*4\*4, 512) in the last block.

TABLE II  
DSE ARCHITECTURES FOR BIGGAN

Block ID Res.	BigGAN Encoder ( $E$ )		
	128×128	256×256	512×512
1 4×4	CBN, CONV(128,128,3), L-ReLU	CBN, CONV(64,64,3), L-ReLU	CBN, CONV(32,32,3), L-ReLU
	CBN, CONV(128,256,3), L-ReLU	CBN, CONV(64,128,3), L-ReLU	CBN, CONV(32,64,3), L-ReLU
2 8×8	CBN, CONV(256,256,3), L-ReLU	CBN, CONV(128,128,3), L-ReLU	CBN, CONV(64,64,3), L-ReLU
	CBN, CONV(256,512,3), L-ReLU	CBN, CONV(128,256,3), L-ReLU	CBN, CONV(64,128,3), L-ReLU
3 16×16	CBN, CONV(512,512,3), L-ReLU	CBN, CONV(256,256,3), L-ReLU	CBN, CONV(128,128,3), L-ReLU
	CBN, CONV(512,512,3), L-ReLU	CBN, CONV(256,512,3), L-ReLU	CBN, CONV(128,256,3), L-ReLU
4 32×32	CBN, CONV(512,512,3), L-ReLU	CBN, CONV(512,512,3), L-ReLU	CBN, CONV(256,256,3), L-ReLU
	CBN, CONV(512,512,3), L-ReLU	CBN, CONV(512,512,3), L-ReLU	CBN, CONV(256,512,3), L-ReLU
5 64×64	CBN, CONV(512,512,3), L-ReLU	CBN, CONV(512,512,3), L-ReLU	CBN, CONV(512,512,3), L-ReLU
	CBN, CONV(512,512,3), L-ReLU	CBN, CONV(512,512,3), L-ReLU	CBN, CONV(512,512,3), L-ReLU
6 128×128	CBN, CONV(512,512,3), L-ReLU	CBN, CONV(512,512,3), L-ReLU	CBN, CONV(512,512,3), L-ReLU
	FC(512×4×4,256), FC(256,128)	CBN, CONV(512,512,3), L-ReLU	CBN, CONV(512,512,3), L-ReLU
7 256×256		CBN, CONV(512,512,3), L-ReLU	CBN, CONV(512,512,3), L-ReLU
		FC(512×4×4,256), FC(256,128)	CBN, CONV(512,512,3), L-ReLU
8 512×512			CBN, CONV(512,512,3), L-ReLU
			FC(512×4×4,256), FC(256,128)

\* CBN is the conditional batch normalization [10] and requires the label vector as input.

\*  $G$  inputs  $\mathbf{z} \in \mathbb{R}^{128}$  and  $\mathbf{c} \in \mathbb{R}^{256}$ , and  $E$  outputs the imitated vectors:  $\mathbf{z}' \in \mathbb{R}^{128}$  and  $\mathbf{c}' \in \mathbb{R}^{256}$ .



Fig. 6. The difference of strategy 1 and 2.

#### IV. EXPERIMENT

To evaluate DSE, we synthesized and reconstructed images from deep GANs, and compared DSE with PGGAN, StyleGAN1, StyleGAN2, and BigGAN ( $x$  vs.  $x'$ ). We also compared DSE with three closely related works: In-Domain GAN [17], ALAE [18], and pSp [19]. Furthermore, we performed an ablation study among different scaled images and latent vectors. Finally, we demonstrated real images with their reconstructions based on DSE. All experiments were implemented (or baseline re-implemented) on PyTorch.

$E$  is trained using the Adam optimizer [41] with a learning rate of 0.0015, and decayed  $\beta$  of ( $\beta_1 = 0$ ,  $\beta_2 = 0.99$ ). We set the number of random samples to 30,000 for each epoch, and we train DSE within 7 epochs. The batch sizes ( $B$ ) for different image sizes are:  $B_{256 \times 256} = 8$ ,  $B_{512 \times 512} = 4$ , and  $B_{1024 \times 1024} = 2$ , which trained on a GPU card (Nvidia Tesla V100-SXM3 32 GB).

##### A. Comparison of Pre-trained GANs

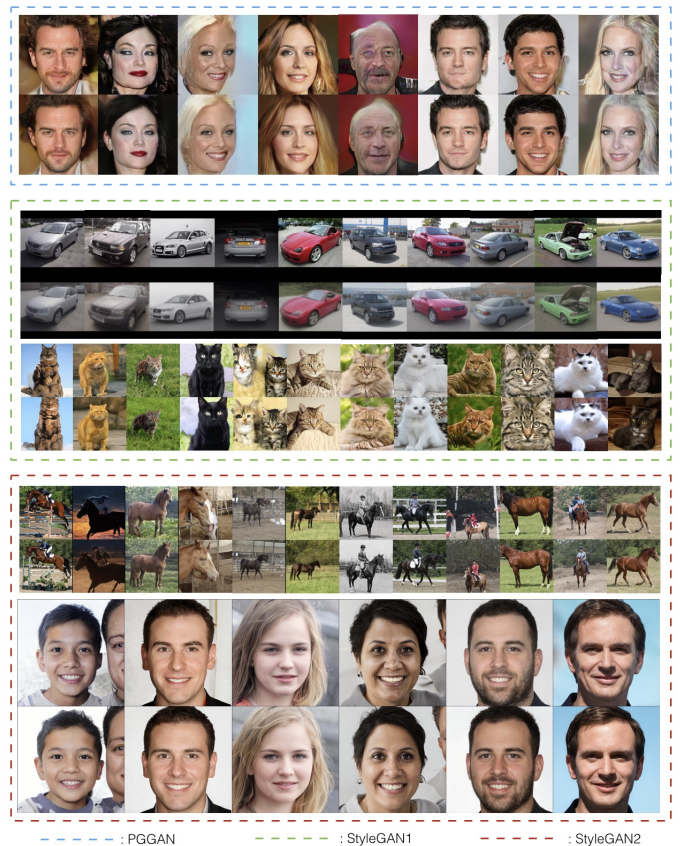
We compared deep GANs with DSE. In BigGAN, DSE fast converged within 5 epochs. The reconstructions are nearly the same as the synthesized images (see Fig. 7). We believe this is due to the additional latent vectors: ImageNet labels (c).

As shown in Fig. 8, reconstructions are better than synthesized images for PGGAN (rows 1-2). We believe that the better results are based on better latent representation via DSE. For StyleGAN1 (rows 3-6), the car's results are slightly more blurred than  $x$ , because here, we only perform strategy 2 in cars.

For StyleGAN2, DSE perfectly reconstructs face images based on the higher GAN performance. Compared with GAN results, the FID score does not improve in the reconstructions, and DSE maintains the same level as the corresponding GANs. DSE reconstructs images well and repairs local areas if they are crumbled or produce unreasonable objects.

##### B. Comparison of Related Works

To compare baselines, we reconstructed  $1024 \times 1024$  real face images. As shown in Fig. 9, the reconstructions of ALAE,

Fig. 7. BigGAN inversions via DSE ( $256 \times 256$ ). Synthesized images (upper) and their reconstructed images (lower).Fig. 8. GAN synthesized images (upper) to DSE reconstructions (lower). There are PGGAN ( $1024 \times 1024$  faces), StyleGAN1 ( $512 \times 512$  cars, and  $256 \times 256$  cats), and StyleGAN2 (LSUN  $256 \times 256$  horses,  $1024 \times 1024$  faces).

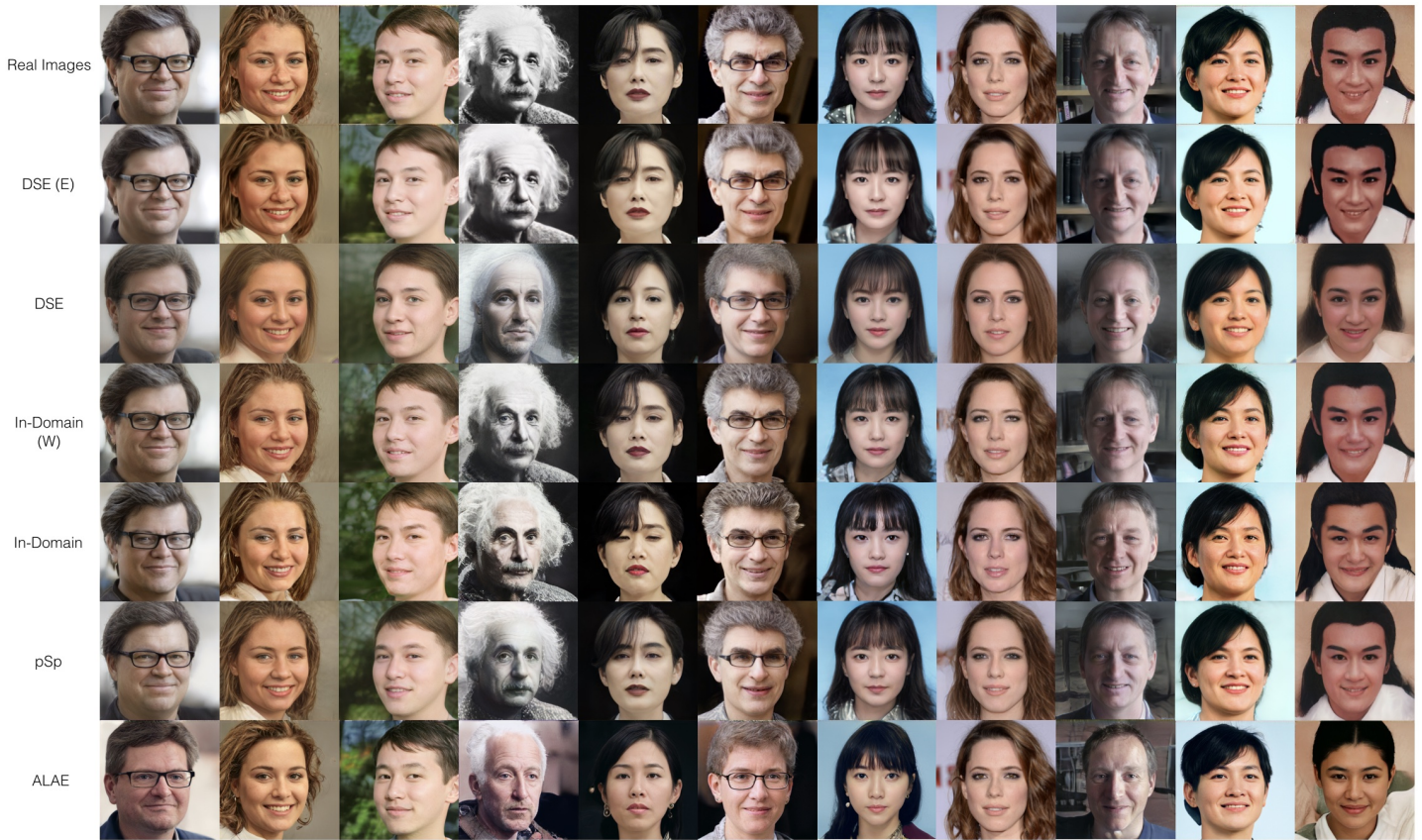


Fig. 9. Visual comparison of baselines with DSE on real face reconstructions.

TABLE III  
COMPARISON OF GAN INVERSION: SYNTHESIZED AND REAL IMAGES.

$x$ vs. $x'$	PSNR $\uparrow$	SSIM $\uparrow$	MSE $\downarrow^{(e2)}$	LPIPS $\downarrow$	CS $\uparrow$
ALAE [18]	15.68	0.497	20.24	0.485	0.77
pSp [19]	21.53	0.640	5.17	0.398	0.94
In-domain [17]	19.53	0.584	8.96	0.422	0.90
DSE	<b>20.45</b>	<b>0.630</b>	<b>6.67</b>	<b>0.368</b>	<b>0.92</b>
$y$ vs. $x'$					
pSp [19]	21.38	0.649	5.12	0.416	0.95
In-domain [17]	19.51	0.599	7.83	0.427	0.92
In-domain (W)	23.45	0.672	3.37	0.367	0.97
DSE	19.12	0.601	8.57	0.421	0.91
DSE (E)	<b>25.92</b>	<b>0.767</b>	<b>1.76</b>	<b>0.293</b>	<b>0.98</b>

pSp, In-Domain, DSE were synthesized directly from pre-trained  $E$ . Similar to Image2StyleGAN [16], In-Domain (W) optimized  $w$  based on encoded results. Different to In-Domain (W), DSE (E) did not directly optimize  $w$ . Instead, DSE (E) optimized  $E$  again, then it is able to output ideal  $w$ .

We evaluated the image similarity from 3,000 random synthesized and real images, where real images were sampled from CelebA-HQ [36]. We report both results in Table III. pSp provides better results for GAN-synthesized images and

is also good for real images. In-Domain (W) is a limited performance by further optimizing  $w$ , and our DSE (E) provides better performance by further optimizing  $E$ .

### C. Ablation Study



Fig. 10. Visual comparison of three-scale centre-aligned images. The 1st row shows generated faces by StyleGAN1 (FFHQ, config F). The 2nd–4th rows show reconstructed images with different scaled attentions (AT1 and AT2).

1) *Three-Scale Images*: Mapping HQ images to latent vectors easily causes inadequate representation, so we selected  $1024 \times 1024$  faces at the 2nd epoch to evaluate the usages of different image scales. For comparison, we trained  $E$



TABLE IV  
ABLATION STUDY FOR SCALED ATTENTIONS.

Reconstructions		PSNR $\uparrow$	SSIM $\uparrow$	LPIPS $\downarrow$	FID $\downarrow$
$x'$	w/o AT	18.97	0.699	0.411	165.45
	w/ AT1	18.82	0.698	0.409	149.34
	w/ (AT1, AT2)	<b>18.75</b>	<b>0.697</b>	<b>0.412</b>	<b>152.80</b>
$x'_1$	w/o ATs	19.65	0.685	0.404	135.34
	w/ AT1	19.76	0.686	0.401	127.25
	w/ (AT1, AT2)	<b>19.71</b>	<b>0.688</b>	<b>0.402</b>	<b>136.48</b>
$x'_2$	w/o AT	20.79	0.701	0.386	101.63
	w/ AT1	20.72	0.699	0.381	87.23
	w/ (AT1, AT2)	<b>21.23</b>	<b>0.712</b>	<b>0.377</b>	<b>86.09</b>

TABLE V  
ABLATION STUDY FOR W/O SSIM.

1,500 iterations	PSNR $\uparrow$	SSIM $\uparrow$	LPIPS $\downarrow$	FID $\downarrow$
w/o SSIM	21.92	0.632	0.395	78.10
w/ SSIM	<b>23.07</b>	<b>0.657</b>	<b>0.396</b>	<b>68.06</b>
3,500 iterations				
w/o SSIM	22.90	0.639	0.386	76.06
w/ SSIM	<b>23.19</b>	<b>0.657</b>	<b>0.393</b>	<b>65.03</b>

via different scaled attentions. We compared mapping performances between different scaled attentions, which are without attentions (w/o AT), one scaled attention (w/ AT1), and two scaled attentions (w/ AT1, AT2).

As shown in Fig. 10, different scaled attentions improve the performance of image reconstructions. We first added AT1 (3rd row); the similarity of the main reconstructive area is better than only using original scaled images (the 2nd row). Then, we added the AT2; the reconstructed similarity is also improved, especially on the key image areas (4th row). Better performances occur when progressively adding the scaled attention. We report the quantitative evaluations at Table. IV (compared with 1500 random samples).

2) *Misaligned Images*: We compared centre-aligned TSA to Gram-CAM-based TSA for misaligned images. We selected  $256 \times 256$  cats to evaluate. The targets (cats) in the image have emerged in the random areas so the images are misaligned. As shown in Fig. 11, in strategy 1, Grad-CAM-based TSA is better than centre-aligned TSA (see rows 2 and 3). In strategy 2, training  $E$  easily fail. Even if we removed  $z_c$  gradients to smooth the training process, but centre-aligned TSA still failed. It is noted that training  $E$  via centre-aligned TSA cannot perform well on misaligned images, e.g., cat eyes (4th row). Gram-CAM-based TSA work well even if in the strict setting: strategy 2 (the last row). Quantitative evaluations are reported at Table. IV (compared with 1500 random samples).

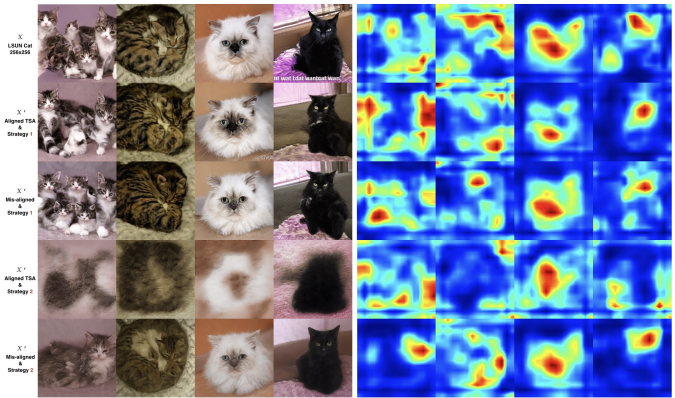


Fig. 11. Visual comparison of three-scale misaligned images among 2 training strategies (StyleGAN2, LSTN Cats).

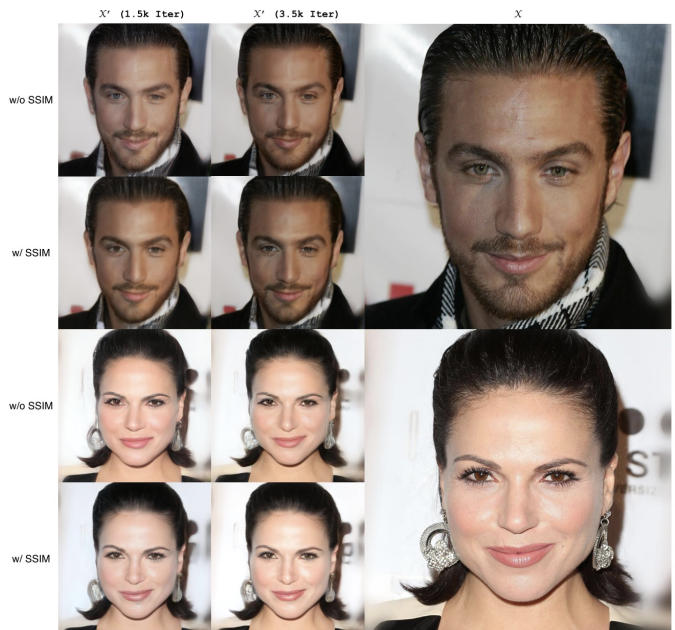


Fig. 12. Visual comparison of w/o SSIM similarity.

3) *w/o SSIM*: Different with previous works [16], [17], [18] whose use MSE and LPIPS to evaluate image similarity, or utilizes face identity model for face similarity [19]. We combine SSIM to evaluate image similarity. The quantitative evaluations are reported at Table. V (compared with 500 real face inversions). Adding SSIM makes better performance on real face inversions. As shown in Fig. 12, at the same iterations, compared with SSIM or without SSIM, SSIM makes better inversion performance.

#### D. Real Image Editing

As shown in Fig. 13, based on DSE inversion, real images can be edited by directly using learned latent directions [21]. Here, real faces were inverted to  $w$ ;  $d$  denotes learned latent direction;  $\alpha$  denotes the  $d$  coefficient. The edited latent vectors denote as  $w' = w + \alpha \cdot d$ .

There is a shortage of HQ real face inversion that local details are blurred in reconstructions (see Fig. 14), such as



Fig. 13. Real face editing.



Fig. 14. The deficiency of GAN inversion for HQ real faces (blur accessories).

earrings and badges. We believe that rare or delicate features are not patterned in SOTA GANs, so these features can not reconstruct well in real faces.

## V. CONCLUSION AND FUTURE WORK

We proposed diverse similarity encoder (DSE), a novel GAN-based approach to invert images to latent space. In latent space, we evaluated similarity of latent vectors so that latent vectors well represent images. For evaluating image similarity, we offered three-scale images to highlight image targets. On aligned images, centre-aligned scaled attentions emphasize outstanding areas. On misaligned images, Grad-Cam-based scaled attentions prominent targets in which the targets appeared in random areas.

DSE has been implemented fine on famous deep GANs (e.g., PGGAN, StyleGAN, and BigGAN). Our quantitative evaluation and visualized results have demonstrated that DSE achieved state-of-the-art performance on deep GAN inversion. Based on DSE, real images can be inverted and edited via latent vectors. In future, learning interpretable directions in latent space for real image editing would be a valuable exploration.

## REFERENCES

- [1] I. Goodfellow, J. Pouget-Abadie, M. Mirza, B. Xu, D. Warde-Farley, S. Ozair, A. Courville, and Y. Bengio, "Generative adversarial nets," in *Proc. Adv. Neural Inf. Process. Syst. (NeurIPS)*, 2014, pp. 2672–2680.
- [2] A. Radford, L. Metz, and S. Chintala, "Unsupervised representation learning with deep convolutional generative adversarial networks," in *Int. Conf. Learn. Representations (ICLR)*, 2016.
- [3] T. Karras, T. Aila, S. Laine, and J. Lehtinen, "Progressive growing of gans for improved quality, stability, and variation," in *Int. Conf. Learn. Representations (ICLR)*, 2018.
- [4] A. Karnewar and O. Wang, "Msg-gan: Multi-scale gradients for generative adversarial networks," in *Proc. IEEE Conf. Comput. Vis. Pattern Recognition (CVPR)*, June 2020.
- [5] T. Karras, S. Laine, and T. Aila, "A style-based generator architecture for generative adversarial networks," in *Proc. IEEE Conf. Comput. Vis. Pattern Recognition (CVPR)*, June 2019.
- [6] T. Karras, S. Laine, M. Aittala, J. Hellsten, J. Lehtinen, and T. Aila, "Analyzing and improving the image quality of stylegan," in *Proc. IEEE Conf. Comput. Vis. Pattern Recognition (CVPR)*, 2020, pp. 8107–8116.
- [7] T. Karras, M. Aittala, J. Hellsten, S. Laine, J. Lehtinen, and T. Aila, "Training generative adversarial networks with limited data," in *Proc. Adv. Neural Inf. Process. Syst. (NeurIPS)*, 2020.
- [8] T. Karras, M. Aittala, S. Laine, E. Härkönen, J. Hellsten, J. Lehtinen, and T. Aila, "Alias-free generative adversarial networks," in *Proc. Adv. Neural Inf. Process. Syst. (NeurIPS)*, 2021, pp. 852–863.
- [9] M. Mirza and S. Osindero, "Conditional generative adversarial nets," *arXiv preprint*, vol. abs/1411.1784, 2014.
- [10] A. Brock, J. Donahue, and K. Simonyan, "Large scale GAN training for high fidelity natural image synthesis," in *Int. Conf. Learn. Representations (ICLR)*, 2019.
- [11] J. Deng, W. Dong, R. Socher, L. Li, K. Li, and F. Li, "Imagenet: A large-scale hierarchical image database," in *Proc. IEEE Conf. Comput. Vis. Pattern Recognition (CVPR)*, 2009, pp. 248–255.
- [12] W. Xia, Y. Zhang, Y. Yang, J.-H. Xue, B. Zhou, and M.-H. Yang, "Gan inversion: A survey," *IEEE Trans. Pattern Anal. Mach. Intell.*, vol. early access, pp. 1–17, 2022.
- [13] J. Donahue, P. Krähenbühl, and T. Darrell, "Adversarial feature learning," in *Int. Conf. Learn. Representations (ICLR)*, 2017.
- [14] A. Creswell and A. A. Bharath, "Inverting the generator of a generative adversarial network," *IEEE Trans. Neural Networks Learn. Syst.*, vol. 30, no. 7, pp. 1967–1974, 2019.
- [15] C. Yu and W. Wang, "Fast transformation of discriminators into encoders using pre-trained gans," *Pattern Recognition Letters*, vol. 153, pp. 92–99, 2022.
- [16] R. Abdal, Y. Qin, and P. Wonka, "Image2stylegan: How to embed images into the stylegan latent space?" in *Proc. IEEE Int. Conf. Comput. Vis. (ICCV)*, 2019, pp. 4431–4440.
- [17] J. Zhu, Y. Shen, D. li Zhao, and B. Zhou, "In-domain gan inversion for real image editing," in *Proc. Eur. Conf. Comput. Vis. (ECCV)*, 2020.
- [18] S. Pidhorskyi, D. A. Adjeroh, and G. Doretto, "Adversarial latent autoencoders," in *Proc. IEEE Conf. Comput. Vis. Pattern Recognition (CVPR)*, 2020.
- [19] E. Richardson, Y. Alaluf, O. Patashnik, Y. Nitzan, Y. Azar, S. Shapiro, and D. Cohen-Or, "Encoding in style: a stylegan encoder for image-to-image translation," in *Proc. IEEE Conf. Comput. Vis. Pattern Recognition (CVPR)*, June 2021.
- [20] J. Donahue and K. Simonyan, "Large scale adversarial representation learning," in *Proc. Adv. Neural Inf. Process. Syst. (NeurIPS)*, 2019, pp. 10 541–10 551.
- [21] Y. Shen, C. Yang, X. Tang, and B. Zhou, "Interfacegan: Interpreting the disentangled face representation learned by gans," *IEEE Trans. Pattern Anal. Mach. Intell.*, 2020.
- [22] C. Yu, W. Wang, H. Li, and R. Bugiolacchi, "2-Step Regularization on Style Optimization for Real Face Morphing," *TechRxiv preprint*, 2 2022.
- [23] H. Li, W. Wang, C. Yu, and S. Zhang, "Swapinpaint: Identity-specific face inpainting with identity swapping," *IEEE Trans. Circuits Syst. Video Technol.*, vol. 32, no. 7, pp. 4271–4281, 2022.
- [24] S. Tulyakov, M. Liu, X. Yang, and J. Kautz, "Mocogan: Decomposing motion and content for video generation," in *Proc. IEEE Conf. Comput. Vis. Pattern Recognition (CVPR)*, 2018, pp. 1526–1535.
- [25] C. Yu, W. Wang, and J. Yan, "Self-supervised animation synthesis through adversarial training," *IEEE Access*, vol. 8, pp. 128 140–128 151, 2020.
- [26] T. White, "Sampling generative networks," in *Proc. Adv. Neural Inf. Process. Syst. (NeurIPS)*, 2016.

- [27] J. Zhu, P. Kr, E. Shechtman, and A. A. Efros, "Generative visual manipulation on the natural image manifold," in *Proc. Eur. Conf. Comput. Vis. (ECCV)*, 2016, pp. 597–613.
- [28] Z. He, W. Zuo, M. Kan, S. Shan, and X. Chen, "Attgan: Facial attribute editing by only changing what you want," *IEEE Trans. Image Process.*, vol. 28, no. 11, pp. 5464–5478, 2019.
- [29] E. Härkönen, A. Hertzmann, J. Lehtinen, and S. Paris, "Ganspace: Discovering interpretable GAN controls," in *Proc. Adv. Neural Inf. Process. Syst. (NeurIPS)*, 2020.
- [30] O. K. Yüksel, E. Simsar, E. G. Er, and P. Yanardag, "Latentclr: A contrastive learning approach for unsupervised discovery of interpretable directions," in *Proc. IEEE Int. Conf. Comput. Vis. (ICCV)*, 2021, pp. 14 243–14 252.
- [31] K. Simonyan and A. Zisserman, "Very deep convolutional networks for large-scale image recognition," in *Int. Conf. Learn. Representations (ICLR)*, 2015.
- [32] A. Krizhevsky, I. Sutskever, and G. E. Hinton, "Imagenet classification with deep convolutional neural networks," *Commun. ACM*, vol. 60, no. 6, pp. 84–90, 2017.
- [33] Zhou Wang, A. C. Bovik, H. R. Sheikh, and E. P. Simoncelli, "Image quality assessment: from error visibility to structural similarity," *IEEE Trans. Image Process.*, vol. 13, no. 4, pp. 600–612, 2004.
- [34] B. Zhou, A. Khosla, A. Lapedriza, A. Oliva, and A. Torralba, "Learning deep features for discriminative localization," in *Proc. IEEE Conf. Comput. Vis. Pattern Recognition (CVPR)*, 2016, pp. 2921–2929.
- [35] R. R. Selvaraju, M. Cogswell, A. Das, R. Vedantam, D. Parikh, and D. Batra, "Grad-cam: Visual explanations from deep networks via gradient-based localization," *Int. J. Comput. Vis.*, vol. 128, no. 2, pp. 336–359, 2020.
- [36] C.-H. Lee, Z. Liu, L. Wu, and P. Luo, "Maskgan: Towards diverse and interactive facial image manipulation," in *Proc. IEEE Conf. Comput. Vis. Pattern Recognition (CVPR)*, 2020, pp. 5549–5558.
- [37] R. Zhang, P. Isola, A. A. Efros, E. Shechtman, and O. Wang, "The unreasonable effectiveness of deep features as a perceptual metric," in *Proc. IEEE Conf. Comput. Vis. Pattern Recognition (CVPR)*, 2018.
- [38] K. He, X. Zhang, S. Ren, and J. Sun, "Deep residual learning for image recognition," in *Proc. IEEE Conf. Comput. Vis. Pattern Recognition (CVPR)*, 2016, pp. 770–778.
- [39] X. Glorot and Y. Bengio, "Understanding the difficulty of training deep feedforward neural networks," in *Proc. Int. Conf. AI. and Stats. (AISTATS)*.
- [40] D. Ulyanov, A. Vedaldi, and V. S. Lempitsky, "Instance normalization: The missing ingredient for fast stylization," *arXiv preprint*, vol. abs:1607.08022, 2016.
- [41] D. P. Kingma and J. Ba, "Adam: A method for stochastic optimization," in *Int. Conf. Learn. Representations (ICLR)*, 2015.